

# Less is More: 1.0 wt% BiBr<sub>3</sub> Enabled a Superlithiophilic Interface on Garnet for Solid-State Batteries

Jiaoli Peng, Zhipeng Wang, Wei Gong, Hongquan Song,\* and Mingpeng Yu\*

Garnet-type Li<sub>6.4</sub>La<sub>3</sub>Zr<sub>1.4</sub>Ta<sub>0.6</sub>O<sub>12</sub> solid-state electrolytes (SSEs) have attracted considerable attention for solid-state lithium metal batteries (SSLMBs) due to their high ionic conductivity, wide electrochemical window, and excellent stability towards lithium. However, poor interfacial contact hinders charge transport and increases impedance. Herein, introducing only 1.0 wt% BiBr<sub>3</sub> into molten lithium at 280 °C in situ forms a mixed ion-electronic conductor (MIEC) of Li<sub>3</sub>Bi and LiBr, significantly enhancing wettability. Thanks to its uniqueness, the modified symmetric cell achieves a remarkably low interfacial resistance (15.7 Ω cm<sup>2</sup>) compared to pristine lithium (1280.3 Ω cm<sup>2</sup>). Furthermore, lithiophilic Li<sub>3</sub>Bi with high ionic conductivity improves the interfacial adhesion and

regulates the Li nucleation. Meanwhile, the lithiophobic LiBr, with high interfacial energy against Li, enables effective suppression of the growth of Li dendrites by promoting the lateral growth of deposited Li metal. Therefore, it achieves a high critical current density (1.4 mA cm<sup>-2</sup>) and stable cycling over 1100 h, at 0.1 mA cm<sup>-2</sup> at room temperature. When paired with a LiFePO<sub>4</sub> cathode, the cell retains 91.6% of its initial capacity after 300 cycles at 0.5 C, demonstrating excellent cycling stability. These findings suggest that the incorporation of 1.0 wt% BiBr<sub>3</sub> effectively constructs a superlithiophilic interface on garnet electrolyte, offering a simple and effective strategy for high-performance SSLMBs.

## 1. Introduction

In the context of the global energy transition towards renewable sources, high-energy-density lithium-ion batteries (LIBs) have become a core driving force in achieving carbon neutrality.<sup>[1,2]</sup> Traditional LIBs use liquid electrolytes, which pose safety risks, such as flammability and leakage.<sup>[3,4]</sup> In contrast, solid electrolytes offer advantages, such as nonflammability and high mechanical strength to suppress the Li dendrite, significantly enhancing the battery safety.<sup>[5–7]</sup> Meanwhile, solid-state lithium-metal batteries (SSLMBs) have been regarded as an ideal choice for achieving high-energy-density batteries due to the use of exceptionally high theoretical specific capacity (3860 mAh g<sup>-1</sup>) and the lowest electrode potential (−3.04 V vs. SHE) of the Li metal anode.<sup>[8,9]</sup> In this regard, high-performance solid electrolytes are the

key enablers for the SSLMB's operation. Nowadays, several kinds of SSEs, including oxide, sulfide, polymer, as well as organic-inorganic hybrid electrolytes have been developed.<sup>[10]</sup> Typically, garnet-based Li<sub>6.4</sub>La<sub>3</sub>Zr<sub>1.4</sub>Ta<sub>0.6</sub>O<sub>12</sub> (i.e., Ta-doped LLZO, LLZT), through lattice structure optimization and lithium-ion migration channel regulation, has attracted intense interest due to much enhanced room-temperature ionic conductivity (up to  $\approx 10^3$  S cm<sup>-1</sup>) and high chemical stability (reduction potential 0.05 V vs. Li/Li<sup>+</sup>).<sup>[11–14]</sup> Moreover, LLZT possesses Young's modulus of 150 GPa and a shear modulus of 60 GPa, both far exceeding the mechanical strength of lithium metal. According to the Monroe-Newman model, LLZT can theoretically suppress lithium dendrite penetration, thereby greatly improving the safety and cycling stability of solid-state batteries.<sup>[15,16]</sup> However, it should be mentioned that the moisture-sensitivity of LLZT can form a lithiophobic lithium carbonate layer spontaneously. Previous studies have proven that LLZT is inherently lithiophilic. However, when exposed to ambient conditions, it inevitably undergoes a Li<sup>+</sup>/H<sup>+</sup> exchange reaction and results in surface residual alkali contamination (e.g., Li<sub>2</sub>CO<sub>3</sub> and LiOH).<sup>[17,18]</sup> This phenomenon significantly reduces the wettability between LLZT and lithium metal, leading to poor interfacial contact. It also induces a porous interface structure filled with microscopic voids, further increasing interfacial impedance. Additionally, the existing structural characteristics cause large fluctuations in local current density and lithium-ion flux, which disrupt uniform deposition/stripping behavior and accelerate dendritic Li nucleation and growth. Eventually, dendritic Li may penetrate the LLZT structure, causing short circuits and battery failure, severely limiting its practical application in high-performance SSLMBs.

Various effective methods have been developed to improve the wettability of molten lithium on LLZT to overcome interfacial

J. Peng, Z. Wang, M. Yu  
Center for Green Innovation  
Beijing Key Laboratory for Magneto-Photoelectrical Composite and  
Interface Science  
School of Mathematics and Physics  
University of Science and Technology Beijing  
Beijing 100083, P. R. China  
E-mail: yum@ustb.edu.cn

W. Gong  
Faculty of Engineering  
Shinshu University  
4-17-1 Wakasato, Nagano-shi 380-8553, Japan

H. Song  
College of Physics and Telecommunication Engineering  
Zhoukou Normal University  
Zhoukou 466001, P. R. China  
E-mail: songhq@zknu.edu.cn

 Supporting information for this article is available on the WWW under <https://doi.org/10.1002/batt.202500240>

challenges. Procedures like mechanical polishing,<sup>[19]</sup> heat treatment,<sup>[20]</sup> or acid treatment<sup>[21,22]</sup> have been used to restore function lost due to contamination. However, SSEs treated with these methods often suffer from lithium loss, structural damage, or the formation of undesirable surface phases. Furthermore, when treated SSEs are re-exposed to atmospheric air, surface contaminants will regenerate immediately. In this regard, the deposition process on the LLZT surface is another effective strategy for optimizing interfacial performance. Techniques, such as chemical vapor deposition (CVD),<sup>[23,24]</sup> atomic layer deposition (ALD),<sup>[25,26]</sup> magnetron sputtering,<sup>[9,27]</sup> and vacuum thermal evaporation (VTE),<sup>[28,29]</sup> are commonly employed to construct functional modification layers on the LLZT surface. However, these physical vapor deposition (PVD) techniques still face various limitations in practical applications, such as low throughput, reduced compositional and orientational control, as well as poor overall conformality. While certain processes require precise control over temperature, pressure, and other parameters, this increases operational complexity and costs. Therefore, despite the excellent deposition capabilities for interfacial modification that have been demonstrated, these techniques remain difficult to commercialize.

To cope with these challenges, molten lithium, composited with specific additives, has emerged as a novel interfacial optimization strategy. Compared to conventional interfacial modification techniques, this proposal does not require high-vacuum equipment, is applicable to large-scale processes, and can be directly integrated into the solid-state battery assembly. In this respect, additives such as strontium nitrides,  $\text{g-C}_3\text{N}_4$ ,<sup>[30]</sup>  $\text{MoO}_3$ ,<sup>[31]</sup> and  $\text{LiNO}_3$ ,<sup>[32]</sup> have been introduced to enhance interfacial wettability, stabilize the chemical environment, and suppress dendritic Li growth. In these cases, the addition of 10 wt% additives were typically adopted. Since lithium has the lowest reduction potential and offers the highest gravimetric energy density, the proportion of additives could have a big impact on the energy density of the cell. How to achieve a superlithiophilic interface, by optimizing the proportion of additives and, at the same time, enhancing the critical current density (CCD), as well as improving the long-term cycling stability, is still a big challenge for garnet-based SSEs, and further research is clearly a requisite to optimize this method. Just recently, a bismuth composite with a strong electronegative halogen element was introduced to improve wetting and contact between LLZT and Li. For instance, Zhou et al.<sup>[33]</sup> reduced the interface resistance to  $7.4 \Omega \text{ cm}^2$  through  $\text{BiF}_3$  modification (20 wt% addition), increased the CCD to  $1.1 \text{ mA cm}^{-2}$ , and stably cycled the lithium symmetric battery for 850 h at a current density of  $0.3 \text{ mA cm}^{-2}$ .

Herein, a Li-BiBr<sub>3</sub> MIEC was constructed through a transformation reaction of commercial BiBr<sub>3</sub> with molten lithium at 280 °C. The in situ-formed Li<sub>3</sub>Bi and LiBr phases with lithium-conducting properties can provide rapid and efficient transport of lithium within the lithium metal electrode. The two together are expected to promote uniform lithium deposition, preventing dendritic Li formation caused by the complex interfacial plating processes between the lithium and the electrolyte.<sup>[34–36]</sup> Furthermore, among LiCl, LiBr, and LiF electrolytes, it has been reported, that LiBr exhibits the highest ion diffusion

coefficient.<sup>[37]</sup> Surprisingly, we find that when the addition amount was controlled at only 1.0 wt%, the Li-BiBr<sub>3</sub> composite exhibited the most obvious effect, which shows the higher critical current density (CCD) value and the lower area-specific resistance (ASR). Due to the specific addition strategy, the constructed solid-state lithium symmetric cell demonstrated a low ASR of only  $15.7 \Omega \text{ cm}^2$ , a high critical current density (CCD) of  $1.4 \text{ mA cm}^{-2}$ , and excellent cycling stability ( $0.1 \text{ mA cm}^{-2}$  for 1100 h) at room temperature. Theoretical density functional theory (DFT) calculations revealed that the LLZT/Li<sub>3</sub>Bi and LLZT/LiBr have much lower interfacial formation energies, signifying an improved interfacial contact between LLZT and lithium. What's more, when the solid-state lithium batteries are paired with LiFePO<sub>4</sub>, a high specific capacity of 156.3 mAh g<sup>-1</sup>, at 0.5 C can be achieved at room temperature, exhibiting favorable rate performance and satisfactory cycling stability. This study provides an attractive solution for addressing the interfacial issues between LLZT and lithium metal electrodes, and regulating the reversible Li plating/stripping behavior, which promotes the practical application of SSLMBs.

## 2. Result and Discussion

In this study, the garnet-type solid-state electrolyte Li<sub>6.5</sub>La<sub>3</sub>Zr<sub>1.5</sub>Ta<sub>0.5</sub>O<sub>12</sub> (LLZT) was synthesized via a conventional solid-state reaction method. X-ray diffraction (XRD, Figure S1, Supporting Information) confirmed that the obtained LLZT exhibits a pure cubic phase (PDF#45-0109), consistent with the findings of Murugan et al. who demonstrated that garnet electrolytes with cubic symmetry possess enhanced lithium-ion mobility.<sup>[38,39]</sup> The dense microstructure of LLZT was further characterized by scanning electron microscopy (SEM, Figure S2, Supporting Information). To evaluate the ionic conductivity, gold films were deposited on both sides of the LLZT pellet via magnetron sputtering, to form blocking electrodes. Electrochemical impedance spectroscopy (EIS) test revealed a room-temperature ionic conductivity of  $5.5 \times 10^{-4} \text{ S cm}^{-1}$ , at 30°C (Figure S3, Supporting Information). Prior to testing, all LLZT samples were mechanically polished using sandpaper (up to 5000 grit) to eliminate surface topographical defects and remove surface contaminants, such as Li<sub>2</sub>CO<sub>3</sub> and LiOH. The pure lithium anode was prepared by melting lithium metal at 280 °C, under an inert argon atmosphere. In this case, Li-BiBr<sub>3</sub> composite lithium anodes were prepared via an alloying method by introducing BiBr<sub>3</sub> at different weight percentages (1.0, 5.0, and 10.0 wt%), denoted as Li-BiBr<sub>3</sub>-1, Li-BiBr<sub>3</sub>-5, and Li-BiBr<sub>3</sub>-10, respectively. Notably, this approach enabled a complete transition from point-to-point contact to conformal contact, between the Li-BiBr<sub>3</sub>-1 anode and LLZT, without requiring additional surface modification of the electrolyte (Figure 1a,b). Interestingly, pure molten lithium exhibited a typical spherical morphology on the LLZT surface (Figure 1c). At the same time, the Li-BiBr<sub>3</sub> melt showed complete spreading behavior in a stainless-steel container (Figure 1d). According to classical surface chemistry, a liquid tends to adopt a spherical shape under static conditions due to surface tension, which minimizes surface area and thus, surface free energy. In metallic liquids, strong

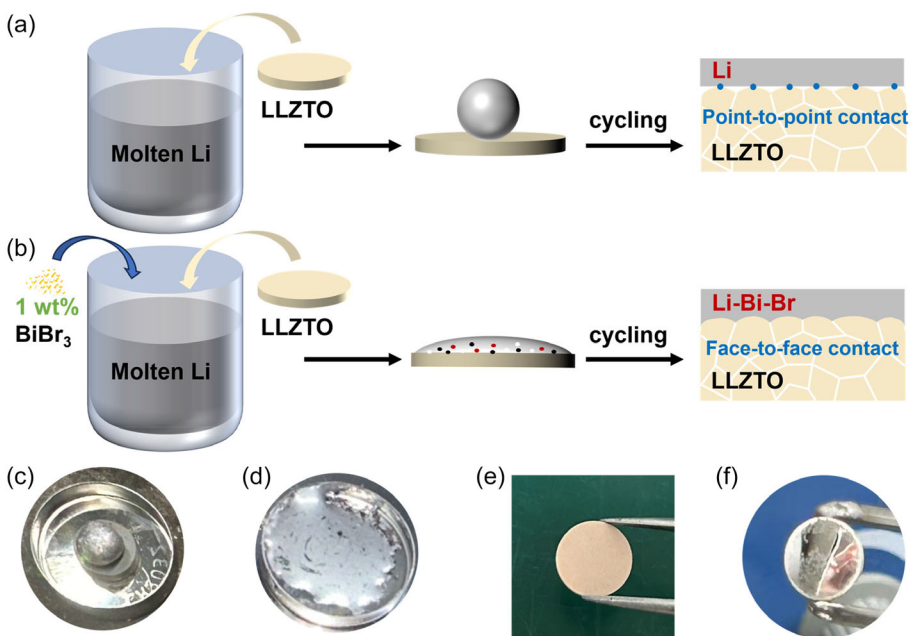


**Figure 1.** Schematic illustration depicting the preparation of a) pure Li melt and b) Li-BiBr<sub>3</sub> melt, along with the resulting interface contact behaviors with garnet pellets. The point-to-point interface contact is converted into a face-to-face contact with the assistance of a 1.0 wt% BiBr<sub>3</sub> modifier. The digital images show c) pure Li melt, d) Li-BiBr<sub>3</sub> melt, e) LLZT garnet pellet, and f) Li-BiBr<sub>3</sub> melt adhering to LLZT.

metallic bonds formed via delocalized electrons result in significantly higher surface tension compared to molecular liquids (e.g., organic solvents), leading to a pronounced contraction behavior.<sup>[40]</sup> Upon the addition of 1.0 wt% BiBr<sub>3</sub>, the Li-BiBr<sub>3</sub> melt demonstrated almost completely uniform spreading across the LLZT surface (Figure. 1e,f), indicating that BiBr<sub>3</sub> effectively reduces the surface tension of the melt lithium metal and improves its wettability behavior upon the LLZT electrolyte.

Due to the strong reducing nature of metallic lithium, redox reactions are expected to occur upon mixing with BiBr<sub>3</sub> powder. In addition, the differences in chemical potentials between BiBr<sub>3</sub> and molten lithium substances could provide fundamental driving forces for triggering reactions. Basically, thermodynamically favorable Li<sub>3</sub>Bi and LiBr will be in situ-generated during the reaction process ( $\Delta H < 0$ , Tab. S1, Supporting Information). The negative value indicates that

the reaction is spontaneous: lithium is bonded more strongly in Li<sub>3</sub>Bi and LiBr than in metallic lithium. To verify the possible chemical product between lithium and BiBr<sub>3</sub>, XRD analysis was conducted to investigate the phase composition of the synthesized mixture. In both cases, pristine BiBr<sub>3</sub> and the prepared Li-BiBr<sub>3</sub> composite were well characterized (Figure 2a). In the Li-BiBr<sub>3</sub> composite, the excess lithium metal exhibits two distinct diffraction peaks located at  $\approx 36.4^\circ$  and  $52.4^\circ$ , corresponding well to the (110) and (200) planes of cubic-phase lithium (PDF#89-7377). All diffraction peaks of pristine BiBr<sub>3</sub> match those in the standard database (PDF#43-0494). After reacting with molten lithium, the characteristic peaks of BiBr<sub>3</sub> completely disappeared, and new diffraction peaks corresponding to Li<sub>3</sub>Bi (PDF#65-8730) and LiBr (PDF#89-3612) emerged, in addition to the peaks from residual lithium. These results confirm the complete reaction between BiBr<sub>3</sub>

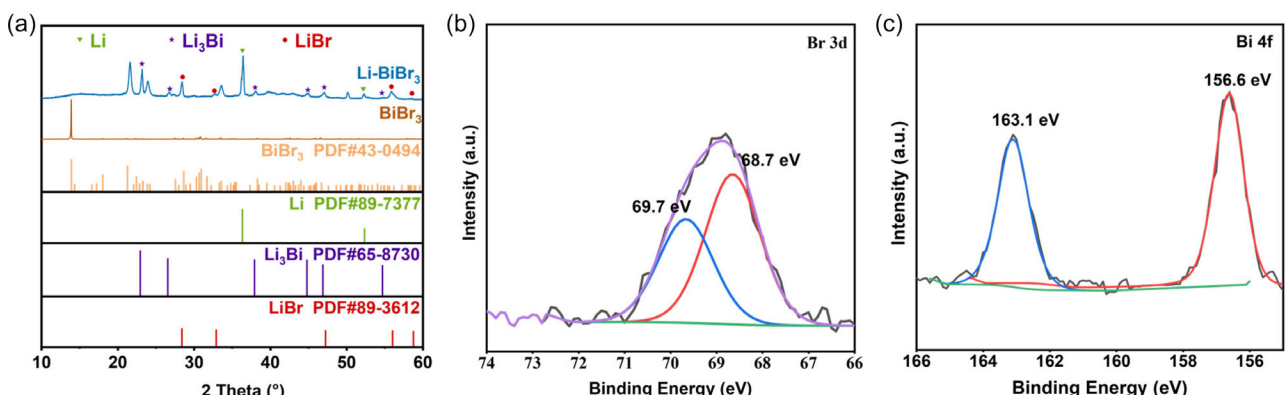


**Figure 2.** a) XRD pattern of Li-BiBr<sub>3</sub> composite. High-resolution XPS spectra of b) Br 3d and c) Bi 4f of Li-BiBr<sub>3</sub> composite.

and molten lithium, leading to the formation of  $\text{Li}_3\text{Bi}$  and  $\text{LiBr}$  phases. To further elucidate the reaction mechanism between  $\text{BiBr}_3$  and lithium metal, X-ray photoelectron spectroscopy (XPS) was performed to analyze the elemental composition and chemical states of the  $\text{Li}-\text{BiBr}_3$  composite (Figure 2b,c). The Br 3 d spectrum (Figure 2b) shows two peaks at 69.4 and 68.3 eV, which are consistent with the binding energies of  $\text{Br}^-$ , indicating that bromine from  $\text{BiBr}_3$  was reduced by lithium to form  $\text{LiBr}$ . The Bi 4f spectrum (Figure 2c) reveals doublet peaks at 163.1 eV and 156.6 eV, suggesting a valence state transition from  $\text{Bi}^{3+}$  to  $\text{Bi}^0$ . Combined with the XRD results, it is confirmed that  $\text{BiBr}_3$  undergoes a complete redox reaction with molten lithium, resulting in the formation of a complex MIEC electrode composed of Li,  $\text{Li}_3\text{Bi}$ , and  $\text{LiBr}$ .

To further understand the effect of 1.0 wt%  $\text{BiBr}_3$  on the wettability of the lithium anode against the LLZT solid electrolyte, DFT calculations were conducted to investigate the interfacial chemical properties of the  $\text{Li}-\text{BiBr}_3$  composite. The calculated interfacial formation energies for  $\text{Li}/\text{LLZT}$ ,  $\text{LiBr}/\text{LLZT}$ , and  $\text{Li}_3\text{Bi}/\text{LLZT}$  interfaces are 1.1, -1.09, and  $-0.87 \text{ J m}^{-2}$ , respectively (Figure 3a–c). The more negative values for  $\text{Li}_3\text{Bi}/\text{LLZT}$  and  $\text{LiBr}/\text{LLZT}$  indicate that the in situ reaction products from  $\text{BiBr}_3$  and molten lithium (i.e.,  $\text{Li}_3\text{Bi}$  and  $\text{LiBr}$ ) facilitate stronger chemical interactions with LLZT, leading to improved interfacial bonding. Coincidentally, He et al. also reported the low cohesive energy of  $\text{LiBr}$  (-26.2 eV), further demonstrating its enhancement of the wettability of molten

lithium on the LLZT electrolyte surface. In this case, lithiophilic  $\text{LiBr}$  possesses high lithium interfacial energy against Li, contributing to the spatial regulation of lithium deposition, and it is believed that this mechanism echoes the principle of LiF-rich SEI layer, which stabilizes the SSE/anode interface and effectively prevents Li dendrites.<sup>[7,41]</sup> Meanwhile, lithophilic  $\text{Li}_3\text{Bi}$  possesses rapid  $\text{Li}^+$  ion transport properties, strong surface adsorption energy, and low surface diffusion barrier, strongly correlated with uniform lithium nucleation and epitaxial growth.<sup>[34,42–44]</sup>

This enhancement in interfacial contact was further validated through cross-sectional SEM characterization. In the SEM images, the upper part corresponds to either pure lithium or  $\text{Li}-\text{BiBr}_3$  composite, while the lower part represents the LLZT pellet. For the pure molten lithium case, significant voids were observed at the interface with LLZT particles, which can be attributed to the high surface tension of molten lithium ( $>400 \text{ mN m}^{-1}$ ) and its strong intrinsic cohesive forces.<sup>[45]</sup> In contrast, the  $\text{Li}-\text{BiBr}_3/\text{LLZT}$  interface exhibits tight and continuous contact without visible interfacial gaps (Figure 3d,e, and Figure S4, Supporting Information). This phenomenon may be mainly attributed to the high ionic conductivity and lithophilic property of  $\text{Li}_3\text{Bi}$ , which allows rapid lithium transport from the bulk phase to the  $\text{Li}-\text{BiBr}_3/\text{LLZT}$  interface, and prevents the formation of voids/cavities, allowing to maintain tight interfacial contact with LLZT during the Li deposition/dissolution process. Energy-dispersive X-ray spectroscopy

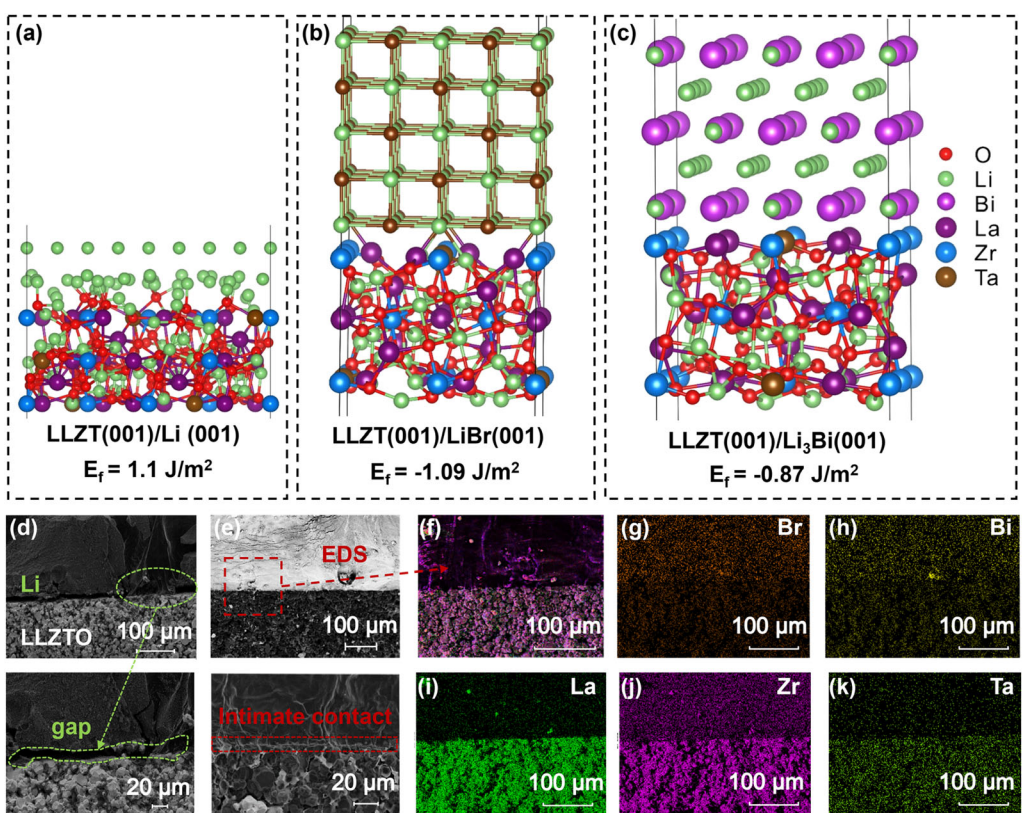


**Figure 3.** DFT calculations of the interfacial formation energies of the a)  $\text{Li}/\text{LLZT}$ , b)  $\text{LiBr}/\text{LLZT}$ , and c)  $\text{Li}_3\text{Bi}/\text{LLZT}$  interfaces. Cross-sectional SEM images of the d)  $\text{Li}/\text{LLZT}$  and e)  $\text{Li}-\text{BiBr}_3/\text{LLZT}$  interfaces at different magnifications. f–k) EDS elemental mapping analysis of the  $\text{Li}-\text{BiBr}_3/\text{LLZT}$  interface.

(EDS) mapping of the Li-BiBr<sub>3</sub>/LLZT interface (Figure 3f-k) further revealed uniform distribution of Bi and Br elements within the lithium matrix and good spatial correlation with interfacial La, Zr, and Ta elements from the LLZT side. It should be noted that due to the detection limit in the EDS analysis, EDS mapping results present different electronic noise intensities. This observation is consistent with the SEM results. Collectively, these findings demonstrate that the incorporation of BiBr<sub>3</sub> effectively enhances the wettability of molten lithium on LLZT particles, resulting in a tightly bonded and conformal Li-BiBr<sub>3</sub>/LLZT interface. Such an interface not only reduces interfacial resistance but also promotes efficient lithium-ion transport across the interface.

Area-specific resistance (ASR) is a critical parameter for evaluating interfacial effectiveness in reducing the severity of stress concentrations. In this study, symmetric cells of Li/LLZT/Li and Li-BiBr<sub>3</sub>/LLZT/Li-BiBr<sub>3</sub> were fabricated to systematically assess the influence of BiBr<sub>3</sub> modification on the interfacial electrochemical properties of garnet-type solid electrolytes. The semicircle

observed in the electrochemical impedance spectroscopy (EIS) plots corresponds to the solid-state interfacial resistance. The intercept on the real axis represents the bulk resistance of the electrolyte. Due to the poor wettability, the ASR of the pristine Li/LLZT/Li cell was as high as 1280.3 Ω cm<sup>2</sup>, while the Li-BiBr<sub>3</sub>-1 cell exhibited a dramatically reduced ASR of only 15.7 Ω cm<sup>2</sup> (Figure 4a), which is also lower than the values reported in several previous studies on garnet-based electrolytes (Tab. S2, Supporting Information). The R1 (R<sub>2</sub>CPE1)-equivalent circuit simulates the EIS of symmetric batteries using pristine lithium and Li-BiBr<sub>3</sub>-1 (Figure 4a). R<sub>1</sub>, R<sub>2</sub>, and CPE1 represent the total resistance of garnet-pellet, interfacial resistance, and capacitor effect, respectively. For comparison, the Li-BiBr<sub>3</sub>-5 and Li-BiBr<sub>3</sub>-10 cells exhibited ASR of about 159.1 and 390.6 Ω cm<sup>2</sup>, respectively (Figure S5, Supporting Information). This could be attributed to the formation of excess Li<sub>3</sub>Bi agglomerates, which is not conducive in the Li ion transportation.<sup>[33]</sup>

The critical current density (CCD), defined as the maximum current density at which the cell can sustain without short-circuiting

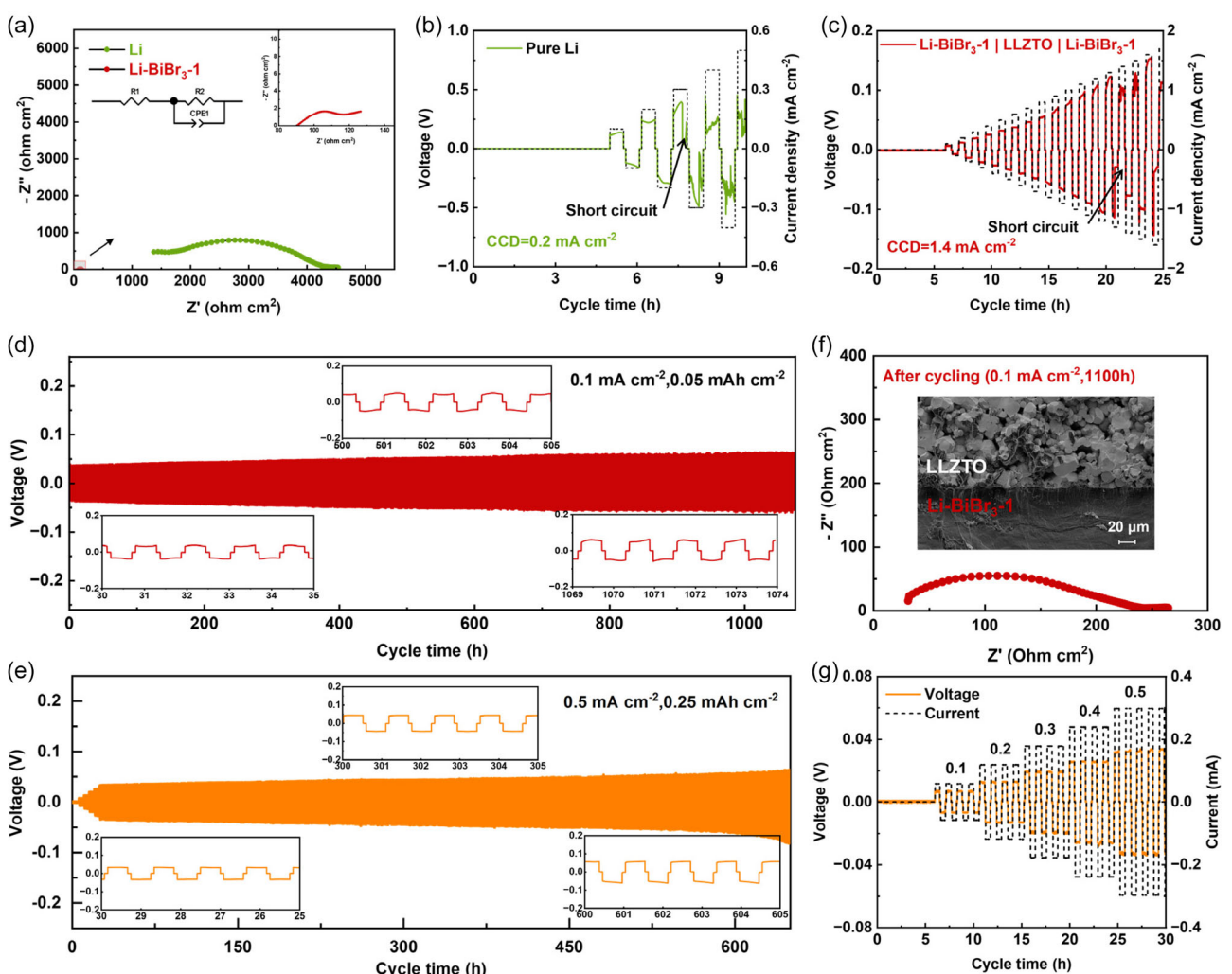


**Figure 4.** a) Comparison of EIS spectra for the Li/LLZT/Li and Li-BiBr<sub>3</sub>-1/LLZT/Li-BiBr<sub>3</sub>-1 cells at room temperature. b,c) CCD for the Li/LLZT/Li and Li-BiBr<sub>3</sub>-1/LLZT/Li-BiBr<sub>3</sub>-1 cells under step-increased current densities. d,e) Li plating and stripping cycling performances of the Li-BiBr<sub>3</sub>/LLZT/Li-BiBr<sub>3</sub> cell at 0.1 and 0.5 mA cm<sup>-2</sup>, along with the corresponding enlarged voltage profiles of Li plating/stripping at different cycling stages. f) EIS spectrum and cross-sectional SEM image of the Li-BiBr<sub>3</sub>-1/LLZT/Li-BiBr<sub>3</sub>-1 cell after being cycled at 0.1 mA cm<sup>-2</sup> for 1100 h. g) Rate performance of the Li-BiBr<sub>3</sub>/LLZT/Li-BiBr<sub>3</sub> cell.

due to lithium dendrite penetration, was also evaluated to prove the interfacial charge transfer capability. CCD measurements were performed under a stepwise, increasing current protocol, with a constant time interval of 30 min. per step. Due to poor interfacial contact, the pristine Li/LLZT/Li symmetric cell experienced a voltage drop and failure at a low current density of  $0.2 \text{ mA cm}^{-2}$  (Figure 4b). In contrast, the Li-BiBr<sub>3</sub>/LLZT/Li-BiBr<sub>3</sub> cell achieved a significantly higher CCD of  $1.4 \text{ mA cm}^{-2}$  (Figure 4c). In comparison, the CCDs of Li-BiBr<sub>3</sub>-5 and Li-BiBr<sub>3</sub>-10 cells were 0.8 and  $0.6 \text{ mA cm}^{-2}$ , respectively (Figure S6, Supporting Information). In addition, galvanostatic cycling tests were conducted to assess the long-term interfacial stability. The pristine Li/LLZT/Li battery rapidly short-circuited after only 40 h of cycling at an ultra-low current density of  $0.015 \text{ mA cm}^{-2}$  (Figure S7, Supporting Information), and the cross-sectional SEM image showed large pores at the interface (Figure S8, Supporting Information). Backscattered electron images captured by SEM clearly showed traces of dendritic Li growth (Figure S9, Supporting Information). In sharp contrast, the Li-BiBr<sub>3</sub>-1/LLZT/Li-BiBr<sub>3</sub>-1 symmetric cell demonstrated stable cycling performance for up to 1100 h at  $0.1 \text{ mA cm}^{-2}$ , and 650 h at  $0.5 \text{ mA cm}^{-2}$  (Figure 4d,e). The voltage profiles during cycling revealed highly stable lithium plating/stripping behavior, with a low overpotential of  $\approx 30 \text{ mV}$  at  $0.1 \text{ mA cm}^{-2}$ . According to the EIS analysis, the interfacial resistance increased only slightly to  $104.3 \Omega \text{ cm}^2$  after prolonged cycling (Figure 4f), indicating that the interface remained well-preserved. Cross-sectional SEM imaging after cycling further confirmed that the Li-BiBr<sub>3</sub>-1/LLZT interface remained tightly bonded without delamination or void formation (Figure 4f). Furthermore, the symmetric cell demonstrated excellent rate performance across a current density range of  $0.1\text{--}0.5 \text{ mA cm}^{-2}$  (Figure 4g). These results clearly indicate that

the incorporation of a small amount of BiBr<sub>3</sub> (1.0 wt%) enables the formation of an intimate and stable interface with the LLZT solid electrolyte, significantly reducing interfacial resistance, and enhancing both CCD and long-term cycling stability. In addition, the interaction (such as lithiophobic and interfacial formation energy) of LiBr with Li could help to explain the additive amount differences and additional research is necessary.

To further validate the practical applicability of the Li-BiBr<sub>3</sub>-1 composite in SSLMBs, full cells were assembled using a LiFePO<sub>4</sub> (LFP) cathode. To mitigate interfacial resistance at the LFP/LLZT interface and promote smooth Li<sup>+</sup> transport, 7  $\mu\text{L}$  of liquid electrolyte (1 M LiPF<sub>6</sub> in EC/DEC, v/v = 1:1) was introduced on the cathode side (Figure 5a). Electrochemical impedance was performed to understand the interfacial stability of the cell. The EIS experiment was conducted between the frequencies of 1 MHz to 0.01 Hz at room temperature. As observed in Figure 5b, the Li-BiBr<sub>3</sub>-1/LLZT/LFP full cell exhibited a total interfacial charge transfer resistance of  $\approx 545 \Omega \text{ cm}^2$ , and only increased to  $1166 \Omega \text{ cm}^2$  after 300 cycles. Moreover, the cell demonstrated excellent rate capability at  $25^\circ\text{C}$  (Figure 5c,d), delivering discharge capacities of  $\approx 157.9, 152.0, 146.8, 127.7$ , and  $112.7 \text{ mAh g}^{-1}$  at 0.1, 0.2, 0.5, 1, and 2 C, respectively. Notably, when the rate was returned to 0.1 C, the discharge capacity recovered to  $157.7 \text{ mAh g}^{-1}$ , indicating good reversibility and rate performance. In terms of long-term cycling stability, the full cell delivered an initial discharge capacity of  $147.3 \text{ mAh g}^{-1}$  at 0.5 C. It retained 91.6% of its capacity after 300 cycles, with a nearly constant coulombic efficiency of  $\approx 99.2\%$  throughout the test (Figure 5e). The high coulombic efficiency also indicates that the interfaces in the full cell were in optimal conditions, and side reactions, including lithium dendrite formation, were prohibited. Furthermore, cycling performance at 0.2 C revealed a capacity

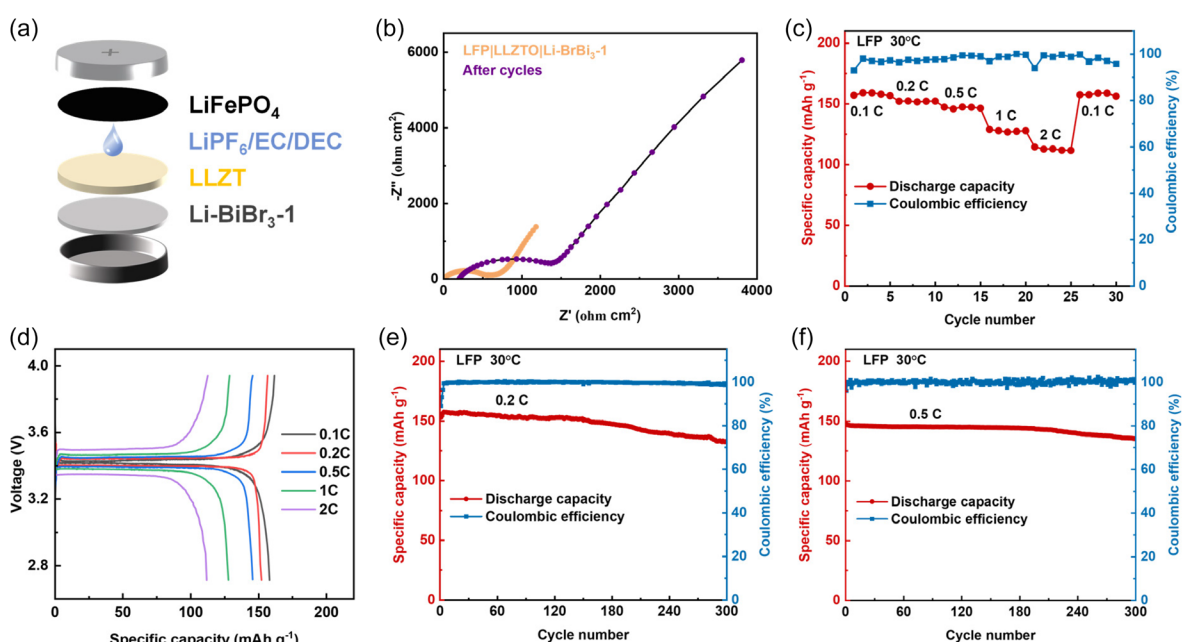


**Figure 5.** a) Schematic representation of the assembly of the all-solid-state Li-BiBr<sub>3</sub>-1/LLZT/LiFePO<sub>4</sub> cell. b) Impedance spectra of the cell before and after cycling at room temperature. c,d) Rate performance and corresponding charge-discharge voltage profiles of the all-solid-state Li-BiBr<sub>3</sub>-1/LLZT/LiFePO<sub>4</sub> cell. e,f) Cycle performance of the Li-BiBr<sub>3</sub>-1/LLZT/LiFePO<sub>4</sub> cell under 0.2 and 0.5 C, at room temperature.

retention of 86.7% after 300 cycles (Figure 5f), confirming the superior electrochemical performance of the Li-BiBr<sub>3</sub>-1 composite anode in SSLMBs.

### 3. Conclusion

In summary, this study investigated the addition of appropriate amounts of BiBr<sub>3</sub> to molten lithium anode. The Li<sub>3</sub>Bi and LiBr phases, and MIEC matrices were in situ generated. With only 1.0 wt% addition, a superlithiophilic interface upon LLZT was successfully developed. DFT calculations reveal that Li<sub>3</sub>Bi and LiBr effectively reduce the interfacial formation energy at the Li/LLZT interface, enabling the Li-BiBr<sub>3</sub> composite to uniformly spread across the LLZT electrolyte surface. As a result, the symmetric cells exhibit a low interfacial resistance (15.7 Ω cm<sup>2</sup>), an excellent critical current density (1.4 mA cm<sup>-2</sup>), and long-term cycling stability (over 1100 h at 0.1 mA cm<sup>-2</sup>) at room temperature, significantly outperforming those based on pristine lithium or other high-content BiBr<sub>3</sub> comparisons (i.e., Li-BiBr<sub>3</sub>-5 and Li-BiBr<sub>3</sub>-10). In addition, full cell paired with LFP cathode demonstrates outstanding rate capability and cycling durability, maintaining 91.6% of the initial capacity after 300 cycles at 0.5 C, with a high coulombic efficiency of ≈99.2% throughout. These performance advantages are attributed to the synergistic effects of Li<sub>3</sub>Bi and LiBr. Both of them can effectively promote uniform lithium deposition and inhibit dendritic Li growth through a stable interfacial structure. Overall, this work offers an innovative and effective strategy to address the interfacial challenges in SSLMBs, and presents a viable route toward the development of high-performance solid-state lithium metal batteries.

### Acknowledgements

This work was supported by Beijing Natural Science Foundation (2212040).

### Conflict of Interest

The authors declare no conflict of interest.

### Data Availability Statement

The data that support the findings of this study are available from the corresponding author upon reasonable request.

**Keywords:** BiBr<sub>3</sub> • garnet-type solid-state electrolytes • mixed ionic–electronic conductors • solid-state lithium metal batteries

- [1] C. Shi, M. Yu, *Energy Storage Mater.* **2023**, *57*, 429.
- [2] J. Lin, X. Zhang, E. Fan, R. Chen, F. Wu, L. Li, *Energy Environ. Sci.* **2023**, *16*, 745.

- [3] M. Wu, S. Han, S. Liu, J. Zhao, W. Xie, *Energy Storage Mater.* **2024**, *66*, 103174.
- [4] J. Xie, Y. C. J. Lu, *Adv. Mater.* **2025**, *37*, 2312451.
- [5] Y.-G. Lee, S. Fujiki, C. Jung, N. Suzuki, N. Yashiro, R. Omoda, D.-S. Ko, T. Shiratsuchi, T. Sugimoto, S. Ryu, *Nature Energy* **2020**, *5*, 299.
- [6] C. Duan, Z. Cheng, W. Li, F. Li, H. Liu, J. Yang, G. Hou, P. He, H. Zhou, *Energy Environ. Sci.* **2022**, *15*, 3236.
- [7] X. Ji, S. Hou, P. Wang, X. He, N. Piao, J. Chen, X. Fan, C. J. Wang, *Adv. Mater.* **2020**, *32*, 2002741.
- [8] K. J. Kim, M. Balaish, M. Wadaguchi, L. Kong, J. Rupp, *Adv. Energy Mater.* **2021**, *11*, 2002689.
- [9] H. Huo, Y. Chen, R. Li, N. Zhao, J. Luo, J. G. P. da Silva, R. Mücke, P. Kaghazchi, X. Guo, X. Sun, *Energy Environ. Sci.* **2020**, *13*, 127.
- [10] L. Fan, S. Wei, S. Li, Q. Li, Y. Lu, *Adv. Energy Mater.* **2018**, *8*, 1.
- [11] C. Wang, K. Fu, S. P. Kammampata, D. W. McOwen, A. J. Samson, L. Zhang, G. T. Hitz, A. M. Nolan, E. D. Wachsman, Y. Mo, V. Thangadurai, L. Hu, *Chem. Rev.* **2020**, *120*, 4257.
- [12] Y. Zhu, X. He, Y. Mo, *ACS Appl. Mater. Interfaces* **2015**, *7*, 23685.
- [13] Q. Guo, F. Xu, L. Shen, S. Deng, Z. Wang, M. Li, X. Yao, *Energy Mater. Adv.* **2022**, *2022*, 9753506.
- [14] C. Shi, S. Takeuchi, G. V. Alexander, T. Hamann, J. O'Neill, J. A. Dura, E. D. Wachsman, *Adv. Energy Mater.* **2023**, *13*, 2301656.
- [15] S. Hu, P. Xu, L. S. de Vasconcelos, L. Stanciu, H. Ni, K. Zhao, *Chinese Phys. Lett.* **2021**, *38*, 098401.
- [16] S. Yu, R. D. Schmidt, R. Garcia-Mendez, E. Herbert, N. J. Dudney, J. B. Wolfenstine, J. Sakamoto, D. J. Siegel, *Chem. Mater.* **2016**, *28*, 197.
- [17] H. Huo, Y. Chen, N. Zhao, X. Lin, J. Luo, X. Yang, Y. Liu, X. Guo, X. Sun, *Nano Energy* **2019**, *61*, 119.
- [18] H. Huo, J. Luo, V. Thangadurai, X. Guo, C.-W. Nan, X. Sun, *ACS Energy Lett.* **2020**, *5*, 252.
- [19] H. Zheng, G. Li, R. Ouyang, Y. Han, H. Zhu, Y. Wu, X. Huang, H. Liu, H. Duan, *Adv. Funct. Mater.* **2022**, *32*, 2205778.
- [20] J. Wu, B. Pu, D. Wang, S. Shi, N. Zhao, X. Guo, X. Guo, *ACS Appl. Mater. Interfaces* **2018**, *11*, 898.
- [21] H. Huo, J. Liang, N. Zhao, X. Li, X. Lin, Y. Zhao, K. Adair, R. Li, X. Guo, X. Sun, *ACS Energy Lett.* **2020**, *5*, 2156.
- [22] Z. Wang, W. Li, S. Jiao, J. Zhu, Z. Wang, J. Peng, W. Gong, J. Wang, H. Huang, H. Song, *Electrochim. Acta* **2024**, *488*, 144242.
- [23] W. Luo, Y. Gong, Y. Zhu, K. K. Fu, J. Dai, S. D. Lacey, C. Wang, B. Liu, X. Han, Y. Mo, *J. Am. Chem. Soc.* **2016**, *138*, 12258.
- [24] W. Feng, X. Dong, X. Zhang, Z. Lai, P. Li, C. Wang, Y. Wang, Y. Xia, *Angew. Chem.* **2020**, *132*, 5384.
- [25] C. Shi, T. Hamann, S. Takeuchi, G. V. Alexander, A. M. Nolan, M. Limpert, Z. Fu, J. O'Neill, G. Godbey, J. A. Dura, *ACS Appl. Mater. Interfaces* **2022**, *15*, 751.
- [26] C. C. Wang, W. C. Hsu, C. Y. Chang, M. Ihrig, N. T. T. Tran, S. k. Lin, A. Windmüller, C. L. Tsai, R. A. Eichel, K. Chiu, *J. Power Sources* **2024**, *602*, 234394.
- [27] L. Zhai, K. Yang, F. Jiang, W. Liu, Z. Yan, J. Sun, *J. Energy Chem.* **2023**, *79*, 357.
- [28] S. Lee, K. S. Lee, S. Kim, K. Yoon, S. Han, M. H. Lee, Y. Ko, J. H. Noh, W. Kim, K. Kang, *Sci. Adv.* **2022**, *8*, eabq0153.
- [29] W. Luo, Y. Gong, Y. Zhu, Y. Li, Y. Yao, Y. Zhang, K. Fu, G. Pastel, C. F. Lin, Y. Mo, *Adv. Mater.* **2017**, *29*, 1606042.
- [30] Y. Huang, B. Chen, J. Duan, F. Yang, T. Wang, Z. Wang, W. Yang, C. Hu, W. Luo, Y. Huang, *Angew. Chem.* **2020**, *132*, 3728.
- [31] B. Liu, M. Du, B. Chen, Y. Zhong, J. Zhou, F. Ye, K. Liao, W. Zhou, C. Cao, R. Cai, *Chem. Eng. J.* **2022**, *427*, 131001.
- [32] G. Lu, M. Li, P. Chen, W. Zheng, Z. Yang, R. Wang, C. Xu, *Energy Environ. Sci.* **2023**, *16*, 1049.
- [33] Z. Li, X. Jiang, G. Lu, T. Deng, R. Wang, J. Wei, W. Zheng, Z. Yang, D. Tang, Q. Zhao, *Chem. Eng. J.* **2023**, *465*, 142895.
- [34] T. Chen, F. Meng, Z. Zhang, J. Liang, Y. Hu, W. Kong, X. L. Zhang, Z. Jin, *Nano Energy* **2020**, *76*, 105068.
- [35] H. Wan, Z. Wang, W. Zhang, X. He, C. Wang, *Nature* **2023**, *623*, 739.
- [36] H. Wan, B. Zhang, S. Liu, J. Zhang, X. Yao, C. Wang, *Nano Lett.* **2021**, *21*, 8488.
- [37] L. Xu, B. Wang, F. Han, S. Liu, P. Sheng, H. Li, G. Zhao, X. Chen, H. Bai, T. Li, *Chem. Phys. Lett.* **2020**, *744*, 137210.
- [38] R. Murugan, V. Thangadurai, W. Weppner, *Angew. Chem. Int. Ed.* **2007**, *46*, 7778.
- [39] X. Huang, J. Tang, Y. Zhou, K. Rui, X. Ao, Y. Yang, B. Tian, *ACS Appl. Mater. Interfaces* **2022**, *14*, 33340.

- [40] K. Zuraiqi, A. Zavabeti, F. M. Allioux, J. Tang, C. K. Nguyen, P. Tafazolymotie, M. Mayyas, A. V. Ramarao, M. Spencer, K. Shah, C. F. McConville, K. K. Zadeh, K. Chiang, T. Daeneke, *Joule* **2020**, *4*, 2290.
- [41] T. Wang, J. Duan, B. Zhang, W. Luo, X. Ji, H. Xu, Y. Huang, L. Huang, Z. Song, J. Wen, *Energy Environ. Sci.* **2022**, *15*, 1325.
- [42] X. Liang, Q. Pang, I. R. Kochetkov, M. S. Sempere, H. Huang, X. Sun, L. F. Nazar, *Nat. Energy* **2017**, *2*, 17119.
- [43] P. Liu, H. Su, Y. Liu, Y. Zhong, C. Xian, Y. Zhang, X. Wang, X. Xia, J. Tu, *Small Struct.* **2022**, *3*, 2200010.
- [44] Y. Xu, H. Zheng, H. Yang, Y. Yu, J. Luo, T. Li, W. Li, Y. N. Zhang, Y. Kang, *Nano lett.* **2021**, *21*, 8664.
- [45] Z. J. Zheng, H. Ye, Z. P. Guo, *Adv. Sci.* **2020**, *7*, 2002212.

---

Manuscript received: March 29, 2025

Revised manuscript received: May 12, 2025

Version of record online: